Polarization-free broadband angular selectivity based on uniaxial zero-refractive-index metamaterials

Zhengjie Huang,[1] Liang Peng,[2,*] Yaqing Huang,[1] Xiaojun Hu,[1] Shenghui Zhao,[3] Xuewei Zhang,[3] Zhiyu Wang,[4,†] Jingxin Tang,[1] Xiaoyu Pang,[3] and Dexin Ye[1,2,‡]

[1] *Laboratory of Applied Research on Electromagnetics, Zhejiang University, Hangzhou 310027, China*
[2] *School of Information and Electrical Engineering, Hangzhou City University, Hangzhou 310015, China*
[3] *AVIC Research Institute for Special Structures of Aeronautical Composite, Aviation Key Lab of Science and Technology on High Performance Electromagnetic Windows, Jinan 250023, China*
[4] *School of Aeronautics and Astronautics, Zhejiang University, Hangzhou 310027, China*

(Received 8 June 2025; revised 27 September 2025; accepted 30 September 2025; published 30 October 2025)

Angle-selective devices that filter electromagnetic (EM) waves from free space are highly desirable for microwave and optical applications. However, most existing designs face challenges in simultaneously achieving a low profile, broad bandwidth, and polarization insensitivity. In this paper, we propose a uniaxial zero-refractive-index metamaterial (UZIM) that offers ultrabroadband transmission under normal incidence while exhibiting narrowband strong reflection for oblique incidence across all polarizations. This unique angular response enables ultrabroadband angular selectivity by cascading UZIM layers with different operating frequencies. By cascading six UZIMs that share the same transmission band under normal incidence but have different reflection bands at oblique incidence, we achieve an angularly selective composite with a 15.56% relative bandwidth. The composite, with a total thickness of $1\lambda_0$, maintains high transmission within 5° of incidence and strong suppression beyond 30° in the whole operating frequency band. The measured results of the fabricated sample show good agreement with full-wave simulations. Our approach addresses the limitations of Brewster-effect-based designs, which suffer from bulky profiles, and overcomes the bandwidth limitations of traditional zero-refractive-index-material-based (ZIM) and frequency-selective-surface-based (FSS) designs. This makes the proposed structure highly suitable for applications such as spatial filtering and antenna sidelobe suppression.

DOI: 10.1103/29pb-mxvf

I. INTRODUCTION

Angle-selective devices transmit electromagnetic (EM) waves efficiently at a specific incident angle and reflect waves from other directions. This unique property attracts considerable interest in both optical and microwave applications, such as antenna sidelobe suppression [1–3], privacy protection [4,5], high-efficiency energy conversion [6], and spatial anti-interference in high-power microwave systems [7–9].

Over the past decades, researchers have developed various strategies to achieve angular selectivity. Among these, geometric optics forms the basis of one approach. For instance, researchers demonstrated a parabolic light-directing microstructure fabricated using two-photon lithography, which transmits only incident light with angles below 5.6° [10]. Similarly, an angle-restricted GaAs solar cell system was designed to minimize the effects of series resistance, achieving a power conversion efficiency exceeding 38% [11].

Zero-refractive-index metamaterials (ZIMs) provide an alternative approach to achieve angular selectivity, typically with a narrow transparency window. For instance, embedding metallic wire arrays into dielectric hosts has enabled the realization of epsilon-near-zero metamaterials with angle-selective properties [12,13]. To eliminate the reliance on metallic components, two-dimensional (2D) multilayer structures have been proposed to achieve similar effects [14,15]. Moreover, an all-dielectric ZIM composed of stacked silicon-rod units has been shown to support directional emission [16]. However, most existing ZIM-based designs are limited to angular selectivity under a single polarization and a narrow bandwidth.

Frequency-selective surfaces (FSSs) offer a promising solution for achieving unpolarized angular selectivity. While early efforts primarily targeted single-polarized designs [17–20], dual-polarized angle-selective transparency has since been demonstrated using engineered

*Contact author: pengl@hzcu.edu.cn
†Contact author: zywang@zju.edu.cn
‡Contact author: desy@zju.edu.cn

double-layer FSS structures [21,22]. In addition, researchers have also investigated angle-selective absorbers, which reflect EM waves at a critical angle while absorbing them at others [23,24]. To improve the bandwidth, a wideband and dual-polarized angle-selective structure using a three-layer configuration has been proposed, obtaining angle-selective transparency with a relative bandwidth of 5% [25]. Despite their benefits, including a low profile and polarization independence, FSS-based designs remain constrained by limited bandwidth due to the relatively narrow passband at the critical angle.

Photonic crystals (PhCs) show broadband transparency at the Brewster angle [26], providing a promising basis for broadband angular selectivity. By stacking multiple PhC layers, the broad passband at the Brewster angle remains unchanged, while off-Brewster angle reflections are significantly enhanced, thereby enabling broadband angular selectivity. Using this Brewster-effect-based principle, Shen *et al.* demonstrated an ultrabroadband design for transverse magnetic (TM) waves using stacked PhC layers [26,27]. To achieve polarization independence, a half-wave plate was employed to convert arbitrarily polarized waves into TM waves [28]. In a more rigorous sense, Gao *et al.* proposed the first polarization-free, broadband Brewster-effect-based design by introducing anisotropic diamagnetic sheets composed of metallic ring arrays [29]. However, due to the inherently low off-angle reflectivity of individual PhC layers, Brewster-effect-based designs require a large number of layers to render sufficient reflection. Thus, even for narrowband operation, the overall structure often reaches a thickness of ten wavelengths, making it impractical for microwave applications.

As wireless systems evolve toward higher capacity and miniaturization, there is a growing demand for angle-selective transparent structures that are low-profile, broadband, and polarization-independent. A promising approach, which advances the Brewster-effect-based strategy, is to create a material layer that inherently exhibits strong angle-selective transparency. Such a layer allows broadband transmission at the critical angle and, more importantly, strong reflection at off-angle incidence. Compared with conventional Brewster-effect-based designs, this approach can achieve sufficient off-angle reflection with the stacking of only a few layers, thereby reducing the overall profile without sacrificing broadband performance or polarization insensitivity.

In this paper, we propose a low-profile, broadband, and polarization-free angular-selective transparent structure. First, we design a uniaxial zero-refractive-index metamaterial (UZIM) that exhibits a broad passband under normal incidence and a narrow reflective stopband under oblique incidence. The passband is achieved using continuous metallic meshes and the stopband is realized by introducing I-shaped resonators and SRRs, which induce near-zero permittivity and permeability along the normal direction, respectively. Next, we design different UZIM layers that share identical passbands but have their stopbands shifted equidistantly in the frequency domain. By cascading these layers with appropriate air spacers, we expand the overall stopband to match the passband spectrum, thereby achieving broadband angular selectivity. Experimental validation using three fabricated UZIM samples shows good agreement with simulations, confirming the effectiveness of the proposed design.

II. THEORETICAL ANALYSIS

The ideal transmission performance of a broadband, polarization-free angle-selective device is shown in Fig. 1(a). The device remains fully transparent to EM waves with incident angles below a critical threshold ($\theta < \theta_t$), while completely reflecting waves at larger incident angles, regardless of polarizations.

To achieve such performance, we begin by analyzing a lossless uniaxial medium characterized by permittivity $\varepsilon = \mathrm{diag}(\varepsilon_t, \varepsilon_t, \varepsilon_n)$ and permeability $\mu = \mathrm{diag}(\mu_t, \mu_t, \mu_n)$. Here, ε_t and μ_t represent tangential components of the permittivity and permeability, respectively, whereas ε_n and μ_n denote their normal components. For both TE waves (with a y-polarized electric field) and TM waves (with a y-polarized magnetic field) propagating along the xoz plane inside the medium, the corresponding dispersion relations are derived as follows:

$$\frac{k_z^2}{\mu_t} + \frac{k_x^2}{\mu_n} = k_0^2 \varepsilon_t, \tag{1}$$

$$\frac{k_z^2}{\varepsilon_t} + \frac{k_x^2}{\varepsilon_n} = k_0^2 \mu_t. \tag{2}$$

Here, k_x, k_y, and k_z represent the wave vector components along the x, y, and z directions, while c is the speed of light and ω is the wave frequency. Given that the dispersion relations for TE and TM waves share the same form, we only discuss the TE case for brevity.

Based on Eqs. (1) and (2), we plot the $\boldsymbol{k}$-surfaces of air and low-μ_n uniaxial medium in the xoz plane. As shown in panel I of Fig. 1(b), the phase-matching condition is satisfied at a small incident angle θ_i and, therefore, the EM waves can be transmitted into the medium. However, for larger θ_i (panel II), the k_x in air exceeds that in the uniaxial medium. Since the continuity of tangential wave vectors is violated, total reflection occurs at the interface. As μ_n approaches zero (or $\varepsilon_n \approx 0$ for TM waves), the range of allowable incident angles narrows, allowing transmission only for near-normal incidence. In addition, the wave impedance of the uniaxial medium under normal incidence is given by $\eta = \eta_0\sqrt{\mu_t/\varepsilon_t}$, where η_0 is the impedance of free space. To achieve perfect impedance matching between air and the medium, the condition $\varepsilon_t = \mu_t$ should be satisfied.

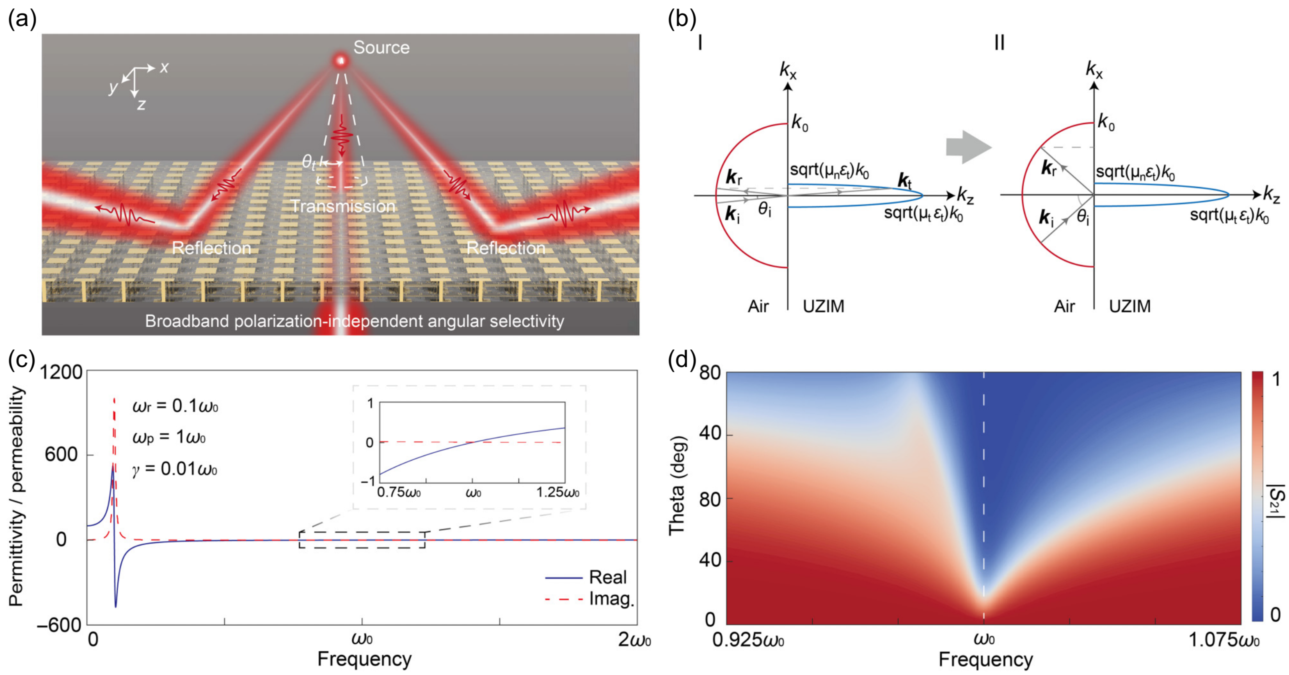

FIG. 1. (a) Ideal transmission performance of broadband, polarization-free angular selectivity. The structure is transparent to EM waves with incident angles $\theta < \theta_t$, while exhibiting highly reflective behavior under other angles. (b) ***k***-surfaces of air and UZIM under small (panel I) and large (panel II) incident angles of the TE waves, illustrating angle-selective transmission due to conservation of tangential wave vector. (c) Dispersion of permittivity with a single Lorentz resonance. (d) $|S_{21}|$ spectrum of an ideal UZIM layer under TE incidence with varying incident angles.

Therefore, a UZIM satisfying both $\varepsilon_t = \mu_t$ and $\varepsilon_n = \mu_n = 0$ exhibits angle-selective transparency at normal incidence for both TE and TM waves. However, these parametric conditions cannot be achieved with naturally occurring materials. Fortunately, metamaterials offer a feasible opportunity to realize such anisotropic behavior, owing to their ability to engineer dispersion along three orthogonal directions [30,31].

The first parametric condition ($\varepsilon_t = \mu_t$) ensures broadband transparency under normal incidence. This condition can be met by using a continuous metallic mesh, which offers a relatively flat permittivity dispersion in the nonresonant region. This property makes it a common choice for achieving broadband transmission [32,33]. The second condition ($\varepsilon_n = \mu_n = 0$) is intended to create a stopband under oblique incidence, which can be realized by introducing a Lorentz resonance. For a single Lorentz resonance, the dispersive permittivity or permeability can be expressed as follows:

$$\varepsilon(\omega) = \varepsilon_0 \left(1 - \frac{\omega_p^2}{\omega^2 - \omega_r^2 + i\omega\gamma}\right), \tag{3}$$

$$\mu(\omega) = \mu_0 \left(1 - \frac{\omega_p^2}{\omega^2 - \omega_r^2 + i\omega\gamma}\right). \tag{4}$$

Here, ω_p, ω_r, and γ represent the plasma frequency, resonance frequency, and damping factor, respectively. The Lorentz dispersion profile is shown in Fig. 1(c), with parameters $\omega_p = 1\omega_0$, $\omega_r = 0.1\omega_0$, and $\gamma = 0.01\omega_0$, where ω_0 denotes the normalized frequency. As can be seen, the permittivity or permeability exhibits a negative response near the resonant frequency. It gradually becomes a positive value at higher frequencies, with a zero-crossing frequency where either permittivity or permeability is zero.

To demonstrate the angular selectivity of the UZIM, we simulate the transmittance spectrum using the ideal parametric setup. For brevity, the analysis is restricted to TE waves. The tangential constitutive parameters are assigned constant values of $\varepsilon_t = \mu_t = 1.5$ across the entire bandwidth, while μ_n follows the dispersive Lorentz model shown in Fig. 1(c). The thickness of the UZIM layer is set to $0.1\lambda_0$, where λ_0 represents the free-space wavelength at ω_0. As shown in Fig. 1(d), near-unity transmittance is achieved under near-normal incidence across the entire bandwidth. However, at larger oblique angles, near-total reflection occurs only at ω_0, which is precisely the zero-crossing frequency of μ_n. The result indicates that the angular selectivity of the UZIM layer remains inherently narrowband, as the resonance-based zero-μ_n condition is always confined to a single frequency. To achieve a broadband design, the stopband bandwidth under

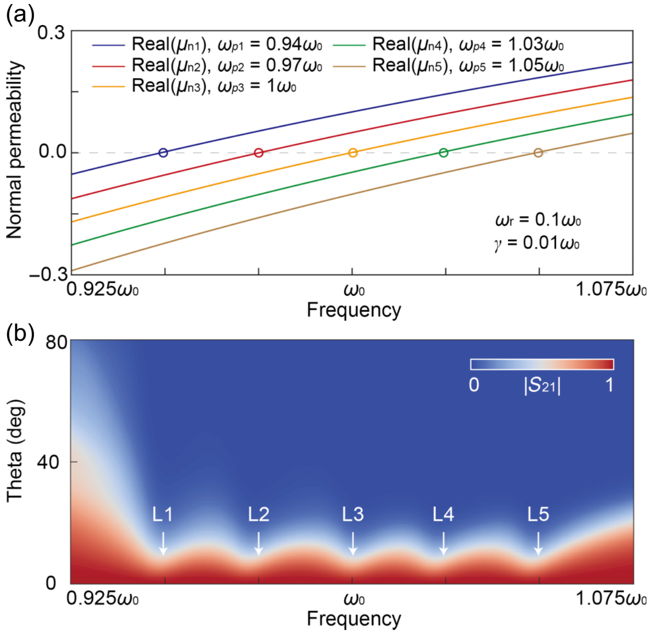

FIG. 2. (a) Relative permeability ($\mu_{\mathrm{n}i}$, $i = 1, 2, \ldots, 5$) along the normal direction (z-axis) for five different UZIM layers. (b) Simulated $|S_{21}|$ for the closely cascaded five-layer structure under TE wave incidence with respect to the incident angle.

oblique incidence must be expanded to match the passband bandwidth under normal incidence.

We propose a multilayer UZIM architecture to broaden the stopband bandwidth. The design consists of five different UZIM layers (L1–L5), each configured with identical tangential constitutive parameters ($\varepsilon_t = \mu_t = 1.5$) but differing normal permeability (μ_n) governed by Lorentz-type dispersion. As shown in Fig. 2(a), the plasma frequencies (ω_{pi}) are set differently across the layers ($\omega_{p1} = 0.94\omega_0$, $\omega_{p2} = 0.97\omega_0$, $\omega_{p3} = 1\omega_0$, $\omega_{p4} = 1.03\omega_0$, and $\omega_{p5} = 1.05\omega_0$), while $\omega_r = 0.1\omega_0$ and $\gamma = 0.01\omega_0$ remain unchanged. Each UZIM layer has a thickness of $0.1\lambda_0$. This parameter setup results in five UZIM layers with spectrally shifted zero-crossings in μ_n, meaning each layer achieves $\mu_n = 0$ at a different frequency.

After cascading these five UZIM layers with $0.026\lambda_0$-thick air spacers, the transmittance of the overall structure under TE waves from 0° to 80° is simulated. As shown in Fig. 2(b), the transmittance is nearly one at near-normal incidence and almost zero at larger incident angles. Compared with the simulation in Fig. 1(d), we observe that the stopbands of each layer effectively combine, resulting in a significant broadening of the overall stopband. Moreover, the operating bandwidth is tunable by simply adjusting the number of UZIM layers to suit practical application requirements.

It should be noted that although cascading multiple layers with distinguished resonances is a common path to realize multiband FSS and metamaterial absorbers [34–36], whose bandwidth extension relies on the strong near-field coupling between adjacent layers, the concept of our design is quite different. The reasons are twofold, as will now be described. (1) As shown in Fig. 1, a single metamaterial layer is designed to be transmissive to the normal incidence but reflective to the oblique incidence. The consequence is that, once illuminated by a Gaussian beam, the metamaterial allows power carried by waves with $\boldsymbol{k}$ nearly normal to pass through but reflects the rest. As the metamaterial layer is generally dispersive, this functionality can only be secured in a limited frequency band. To extend the operational band, multiple metamaterial layers are stacked together to reflect oblique incidence at varied frequencies, while maintaining normal transmission unaffected. So, the working mechanics of our design is not resonance-dependent in principle, although the nearly zero permittivity or permeability has to be generated through the Lorentz oscillation of the media. (2) As we previously stated that each layer would reflect oblique incidence at a certain frequency, it is expected that the stacking of multiple layers should have little influence on the functionality of individual layers. Hence, strong near-field coupling between adjacent layers should be deeply suppressed to ensure the quality of reflection and transmission, which differs from conventional wideband FSS and absorbers.

The above analysis numerically validates our design approach. In the following sections, we provide a detailed description of the actual UZIM design and demonstrate how cascading multiple UZIM layers enables broadband operation.

III. DESIGN AND SIMULATION

A. UZIM design

As shown in Fig. 3(a), a bilayer continuous metallic mesh is employed to produce a flat electric resonance and achieve broadband transmission under normal incidence [32,33]. To tailor the response under TE-polarized oblique incidence, SRRs are introduced into the unit cell [Fig. 3(b)], which couples to the normal component of the magnetic field and thereby controls the normal permeability ($\mu_z \approx 0$). To manipulate the normal permittivity ($\varepsilon_z \approx 0$), metallic vias are embedded through the dielectric substrate and connected to metallic patches at both ends, forming an I-shaped electric resonator along the z-direction [Fig. 3(c)]. The final unit cell [Fig. 3(d)] integrates the continuous metallic mesh, SRRs, and I-shaped resonators, enabling three-dimensional (3D) dispersion engineering. This integration is essential for realizing the desired constitutive parameters, i.e., the transverse components satisfy $\varepsilon_t \approx \mu_t$ and the normal components approach $\varepsilon_n \approx \mu_n \approx 0$.

The UZIM is designed to operate within the C-band, a frequency range widely utilized in wireless systems. Simulations are conducted using CST MICROWAVE STUDIO,

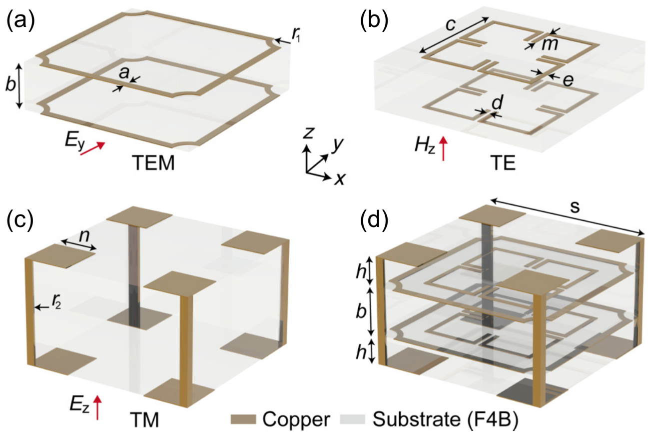

FIG. 3. Unit cell of the UZIM layer. (a) Bilayer continuous metallic mesh responding to a tangentially polarized electric field. (b) SRRs responding to a normally polarized magnetic field. (c) I-shaped resonators responding to a normally polarized electric field. (d) Finalized unit cell.

where periodic boundary conditions are applied along the x and y directions of the unit cell to emulate an infinite slab. As illustrated in Fig. 3, the substrate (gray region) is modeled using F4B dielectric material, characterized by a relative permittivity of 2.55 and a loss tangent of 0.002. The metallic components (brass regions) are represented as 0.035-mm-thick lossy copper with a conductivity of 5.8×10^7 S/m. After optimization, the unit cell is tuned to operate at 7.6 GHz, with the final geometric parameters defined as follows: $a = 0.4$ mm, $b = 2$ mm, $c = 5.8$ mm, $d = 0.16$ mm, $h = 1$ mm, $e = 0.2$ mm, $m = 1.72$ mm, $s = 7.6$ mm, $n = 2.68$ mm, $r_1 = 0.75$ mm, and $r_2 = 0.3$ mm. These optimized dimensions enable the UZIM to achieve polarization-free angular selectivity. In particular, Appendix C provides a detailed analysis of how the primary in-plane dimensions (a, m, and n) influence the angular selectivity and operating bandwidth of the UZIM layer.

To clarify the design mechanism, we analyze the surface current distributions at 7.6 GHz under different incident conditions. Under normal incidence with the electric field polarized along the y-direction, the surface current is primarily confined to the continuous metallic mesh, as shown in Fig. 4(a). This indicates that the tangential permittivity can be effectively tuned by adjusting the geometric parameters of the mesh. Under oblique TE incidence at 45°, where the normal component of the magnetic field is present, strong surface currents are observed on the SRRs [Fig. 4(b)], enabling control of the normal permeability. In the case of oblique TM incidence at 45°, where a normal component of the electric field is involved, intensive surface currents are induced on the z-oriented I-shaped resonators [Fig. 4(c)], thereby facilitating modulation of the normal permittivity.

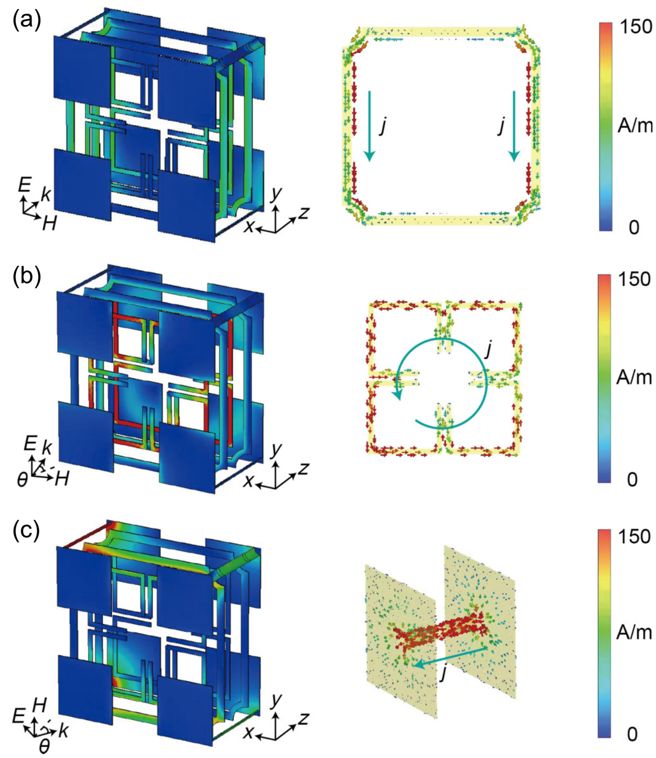

FIG. 4. Surface current distributions at 7.6 GHz under different incident waves: (a) under normal incidence with a y-polarized electric field, (b) under TE oblique (45°) incidence with a y-polarized electric field, and (c) under TM oblique (45°) incidence with a y-polarized magnetic field.

Since the thickness of the proposed UZIM is less than one-ninth of the operating wavelength, its EM properties can be accurately characterized using effective medium theory. The effective constitutive parameters are extracted using a robust retrieval method [37]. As shown in Fig. 5(a), the retrieved parameters at 7.6 GHz are $\varepsilon_r = \mu_r = \mathrm{diag}(1.35,\ 1.35,\ 0)$, which fulfill the material criteria required for achieving angular selectivity.

Figure 5(b) shows the transmission coefficient ($|S_{21}|$) under various incident angles. Under normal incidence, the proposed UZIM exhibits a broad passband with $|S_{21}|$ exceeding 0.9. In contrast, under oblique incidence, a narrow stopband emerges near 7.6 GHz for both polarizations. Figure 5(c) further presents the variation of $|S_{21}|$ at 7.6 GHz as a function of incident angle, demonstrating that the UZIM maintains high transparency ($|S_{21}| > 0.9$) for both polarizations within the 0°–5° range. Beyond 30°, $|S_{21}|$ drops below 0.3, showing a narrow angular transparency window.

To visually evaluate the angular selectivity of the UZIM, we simulated the EM field distributions around the structure under different incidence conditions. Figure 6(a) displays the electric field distributions at 7.6 GHz for both normal incidence and 30° TE-polarized incidence, while

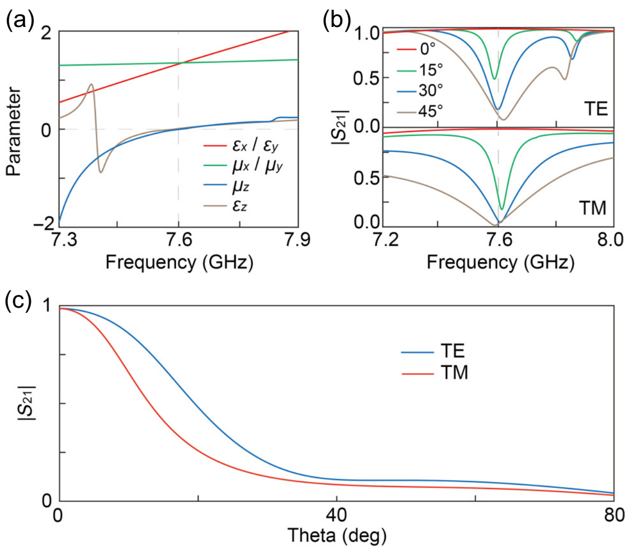

FIG. 5. (a) Retrieved constitutive parameters of the UZIM layer. (b) Simulated $|S_{21}|$ versus frequencies under TE and TM wave incidences. (c) Simulated $|S_{21}|$ at 7.6 GHz with varying incident angles.

Fig. 6(b) presents the corresponding magnetic field distributions for the TM case. The results demonstrate that the UZIM exhibits high transparency under normal incidence, while reflecting nearly all the incident power at 30° incidence, regardless of polarization.

It should be noted that the angular selectivity shown in Figs. 5 and 6 seems to be different for TE and TM waves. Generally, for an ideal homogeneous material possessing identical permittivity and permeability tensors, the angular responses should be the same for TE and TM waves. However, the metamaterial unit cells have a particular structure with finite dimensions, which leads to angular dispersion for different polarizations. Yet, for a given unit cell size, the extent of angular dispersion also depends on the oscillation mechanism [38–40]. In this work, the magnetic SRR and the I-shaped electric resonator are utilized to generate magnetic and electric resonances, exhibiting distinct spatial responses and quality factors. Consequently, the proposed UZIM inevitably responds differently to TE and TM polarizations. Two possible approaches may be used to minimize the angular selectivity difference for the two polarizations. The first approach is to further reduce the overall size of the unit cells by incorporating lumped elements. The second approach is to match the spectral dispersion of both the electric and magnetic resonances, although this operation is rather challenging.

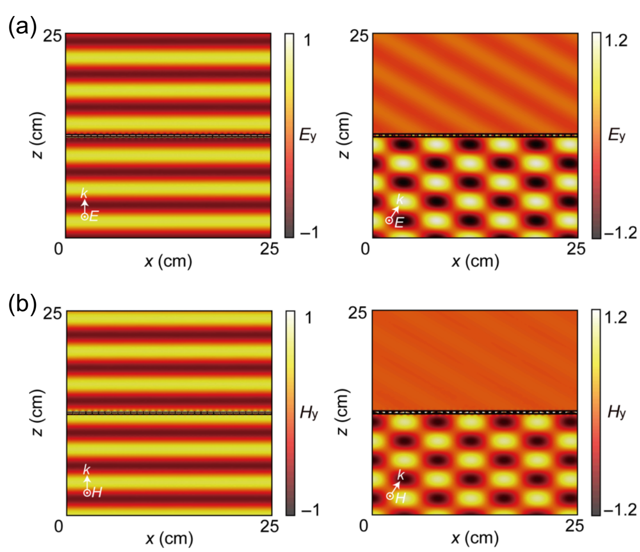

FIG. 6. (a) Simulated electric field distributions around the UZIM layer under 0° and 30° TE plane wave incidence with a y-polarized electric field. (b) Corresponding magnetic field distributions under TM plane wave incidence with a y-polarized magnetic field.

B. Bandwidth broadening

To demonstrate the bandwidth broadening effect, we design three UZIM layers, labeled U1, U2, and U3. For simplicity, U1 retains the previous design operating at 7.6 GHz (as shown in Fig. 5). By modifying the dimensions of the SRRs and I-shaped resonators, we shift the zero-μ_z and zero-ε_z frequencies of U2 and U3 to 7.8 GHz and 8.0 GHz, respectively. The simulated $|S_{21}|$ for U2 and U3 are presented in Fig. 7(a) and 7(b), respectively. As observed, all three UZIMs exhibit a nearly identical broad passband under normal incidence, while producing distinct narrow stopbands under oblique incidence. The detailed geometric parameters for the three designs are listed in Table I.

Next, three UZIM layers (U1, U2, and U3) are stacked with 3-mm air spacers to form a composite structure. As shown in Fig. 7(c), the composite maintains high transmittance ($|S_{21}| > 0.9$) under normal incidence across the 7.4–8.2 GHz frequency range. The maximum insertion loss within the passband (7.4–8.2 GHz) is 0.42 dB. A slight reduction in transmittance is observed compared with a single UZIM layer, primarily due to the accumulated material losses from the multiple layers. Notably, under 30° oblique incidence, the individual narrow stopbands of the three layers merge to form a significantly broadened stopband spanning 7.6–8.0 GHz. It is important to note that this stopband broadening effect is sensitive to EM coupling between adjacent UZIM layers, necessitating careful optimization of the air-gap thickness. To minimize coupling while maintaining a compact structure, the air gap is set at $t = 3$ mm.

Clearly, the maximum angle-selective bandwidth achievable with the proposed approach depends on the passband bandwidth ($|S_{21}| > 0.9$) under normal incidence. By adding additional UZIM layers, the stopband can be

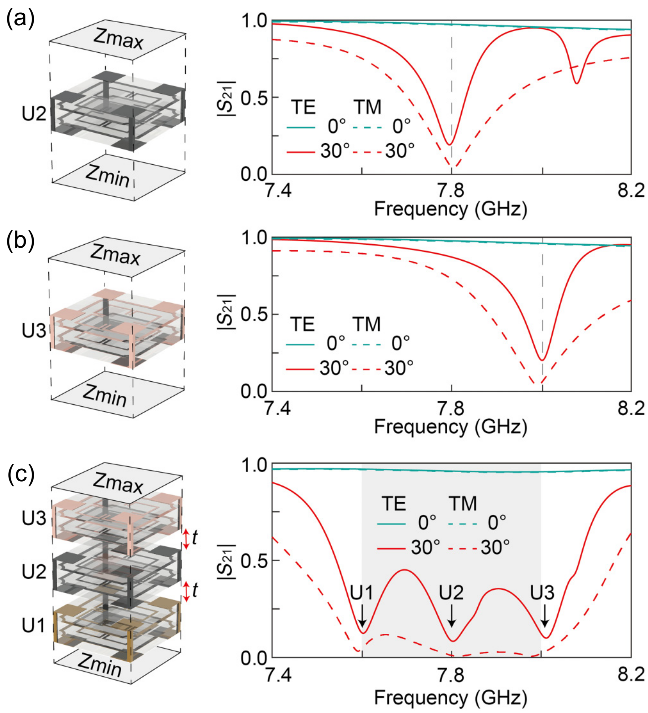

FIG. 7. Simulated $|S_{21}|$ for different UZIM layers under 0° and 30° incidences of TE and TM waves. (a) Results for a single UZIM layer (U2) with its operating frequency of 7.8 GHz. (b) Results for a single UZIM layer (U3) with its operating frequency of 8 GHz. (c) Results for the cascaded three-layer (U1, U2, and U3) structure, where the air gap between two adjacent layers is 3 mm ($t = 3$ mm).

further broadened to align with the full extent of the passband. As illustrated in Fig. 8, a polarization-free, angle-selective response with a relative bandwidth of 15.56% (ranging from 7.1 to 8.3 GHz) is achieved using a six-layer UZIM stack. Each layer is individually tuned to operate at a distinct frequency: 7.2, 7.4, 7.6, 7.8, 8.0, and 8.2 GHz. The detailed geometric parameters for all six UZIM layers are provided in Table I. The resulting composite structure exhibits a broad passband ($|S_{21}| > 0.9$), for incident angles below 5°, and the maximum insertion loss within the passband (7.1 to 8.3 GHz) under normal incidence is around 0.95 dB, while effectively suppressing transmission ($|S_{21}| < 0.3$) for angles greater than 30°. However, in the

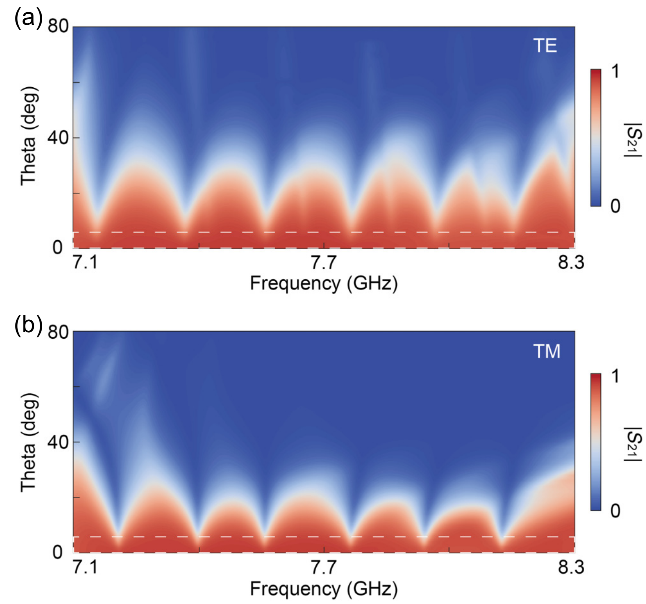

FIG. 8. Simulated $|S_{21}|$ spectrum for the cascaded six-layer structure, with the operating frequencies of the six UZIM layers at 7.2, 7.4, 7.6, 7.8, 8, and 8.2 GHz: (a) under the TE wave incidence and (b) under the TM wave incidence.

intermediate range, the uniformity of angular selectivity is not satisfactory. This is primarily determined by the size of the frequency spacing (0.2 GHz in this design) between two adjacent resonances. The overall angular selectivity uniformity can be improved by reducing the frequency spacing. In such a case, the intermediate angular range can also be suppressed (see Appendix D for more details).

Compared with the results for the three-layer structure, the insertion loss under normal incidence for the six-layer one increases nonlinearly. According to the full-wave simulated result, this insertion loss primarily originates from material losses in both the metal and the dielectric (see Appendix B for more details), where the metal loss dominates. It might be feasible to reduce the insertion loss by replacing the metallic resonators with all-dielectric ones, such as the BIC-inspired all-dielectric resonators [41,42].

We provided above a detailed demonstration of the actual UZIM design, showing how cascading multiple layers achieves a broad bandwidth. Overall, the bandwidth

TABLE I. Geometric parameters (mm) of six UZIMs.

Unit cell	A	b	c	d	e	m	n	h	s	r_1	r_2
U1	0.4	2	5.8	0.16	0.2	1.72	2.68	1	7.6	0.75	0.3
U2	0.35	2	5.8	0.16	0.2	1.58	2.68	1	7.6	0.75	0.32
U3	0.32	2	5.8	0.16	0.2	1.47	2.68	1	7.6	0.75	0.35
U4	0.32	2	5.8	0.16	0.2	1.38	2.68	1	7.6	0.75	0.38
U5	0.382	2	5.8	0.16	0.2	1.82	2.7	1	7.6	0.75	0.27
U6	0.4	2	5.8	0.16	0.2	1.96	2.7	1	7.6	0.75	0.24

is highly dependent on the total device thickness, which is directly proportional to the number of cascaded layers. Therefore, there are some tradeoffs primarily lying among the angular rejection range, the number of cascaded layers, and the operating bandwidth in an actual design. For example, a larger angular rejection range results in a narrower bandwidth for a given number of cascaded layers. For a specific angular rejection range, a wider bandwidth requires a greater number of layers. Certainly, the stacking of multiple metamaterial layers is also limited due to some practical issues. First, considering that the metamaterial layers are composed of metallic structures, the spacing between adjacent layers should be ensured to avoid strong near-field coupling, which leads to an increase in the total thickness of the whole structure when the number of layers is large. In Appendix D, we provide a detailed analysis of how the air gap between two adjacent layers is chosen. Second, the operating bandwidth of a single-layer transmissive metasurface under normal incidence imposes a fundamental limit—no matter how many layers are stacked, the overall bandwidth cannot exceed that of a single layer. Third, the inherent material losses (i.e., ohmic loss in metals and dissipation in dielectrics) will nonlinearly grow with a large number of layers. A more detailed demonstration of these tradeoffs can be found in Appendix A.

IV. EXPERIMENT AND DISCUSSION

To experimentally validate the EM performance of the proposed design, we fabricated samples based on the three simulated UZIMs (U1, U2, and U3) using standard printed circuit board (PCB) technology. As shown in Fig. 9(a), each sample consists of $52 \times 21 \times 1$ unit cells, with overall dimensions of $523 \times 213 \times 4$ mm^3. The structure comprises four 0.035-mm-thick copper layers and three F4B dielectric substrates (two 1-mm layers and one 2-mm layer). The metallic patterns are periodically etched onto the substrates, which are then laminated together with adhesive bonding. Finally, metallic vias are drilled through the entire structure to connect the top and bottom copper layers electrically.

The transmission measurements are conducted in a microwave anechoic chamber. A pair of C-band horn antennas is used for both transmitting and receiving, with an Agilent 8722ES network analyzer connected to each antenna to measure $|S_{21}|$. The antennas are positioned 3 meters apart to minimize near-field coupling effects.

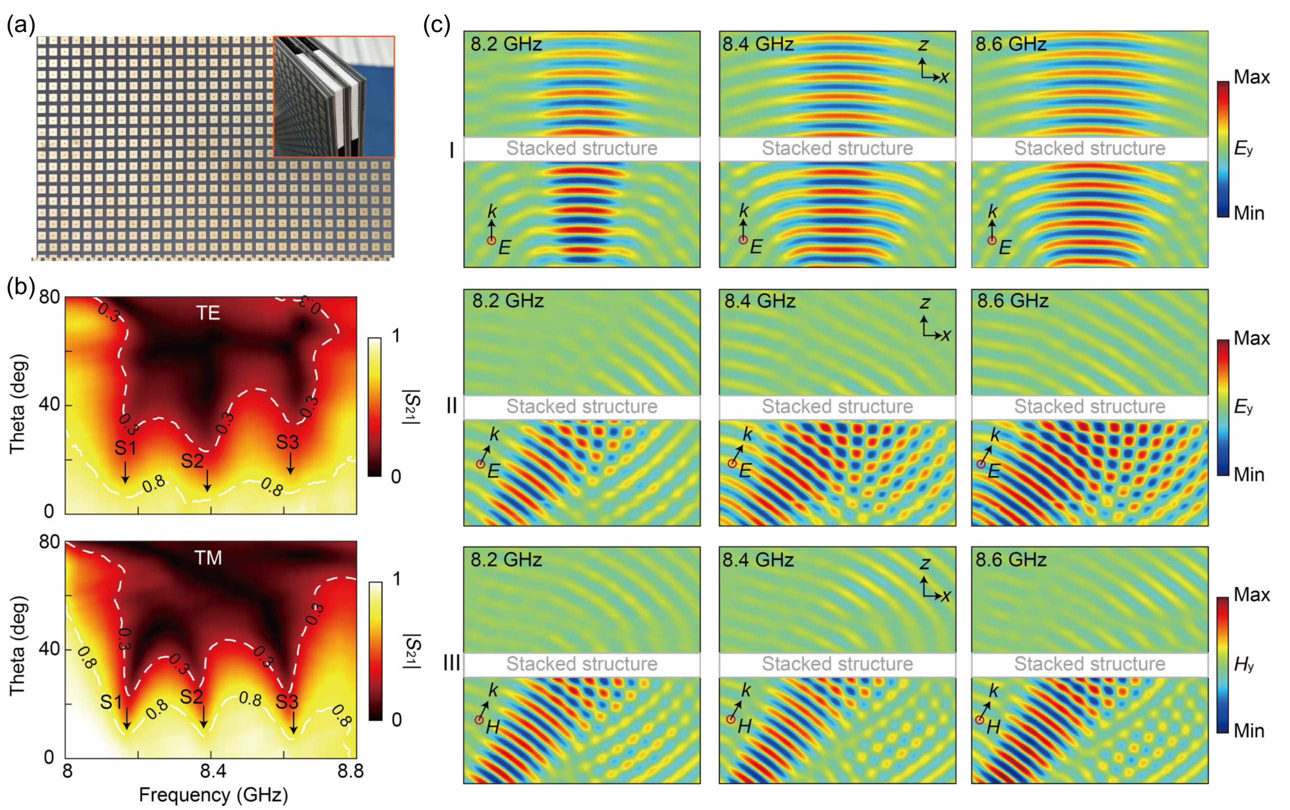

FIG. 9. (a) Front and side views of the cascaded composite. (b) Measured $|S_{21}|$ of the cascaded sample for the TE and TM waves. (c) Measured field distributions around the cascaded sample at 8.2, 8.4, and 8.6. Panel I: normal incidence. Panel II: oblique (30°) TE wave incidence. Panel III: oblique (30°) TM wave incidence.

The fabricated samples, surrounded by absorber material, are placed on a rotation stage located at the midpoint between the antennas. By adjusting the orientation of the antennas and rotating the stage, both the polarization and the incident angle of the EM wave can be systematically varied.

In the experiment, three fabricated samples (S1, S2, and S3) are stacked to form a composite structure, with each layer separated by a 4-mm-thick airlike foam. Figure 9(b) presents the measured $|S_{21}|$ of the composite structure under TE and TM incidence. The individual operating frequencies of the three samples are approximately 8.2, 8.4, and 8.6 GHz. At these frequencies, the composite achieves a transmittance greater than 0.8 within an incident angle range of 0°–8° for both polarizations. As the incident angle exceeds 38°, the transmittance decreases to 0.3. Notably, the stopbands of the individual samples under oblique incidence merge to produce a broadened overall stopband. The composite sample exhibits polarization-free, broadband angular selectivity, which effectively agrees with the simulation results.

It should be noted that the discrepancy between the measured and simulated operating frequencies may be attributed to fabrication tolerances and variations in the dielectric constant of F4B. In Appendix C, we provide a detailed analysis of the tolerances in the geometric parameters. It is seen that the geometric tolerances of both the electric and magnetic metallic resonators are relatively tight. Besides, the experimentally measured transmittance within the passband is lower than the simulated values. This reduction is likely due to higher actual losses in the copper and F4B materials compared with the parameters used in the simulations. Moreover, the bonding film used during the lamination process also introduces additional dielectric loss.

To show the performance of the samples in the spatial filter scenario, we measured the surrounding EM field distributions around the cascaded structure, as illustrated in Fig. 9(c). In the measurement, the transmitting horn antenna is placed approximately 60 cm from the cascaded sample to generate TE and TM waves at incident angles of 0° and 30°, mimicking signals originating from free space. For TE incidence, a monopole antenna is used as a probe to measure the y-polarized electric field in the xoz plane. For TM incidence, a small loop antenna is applied to capture

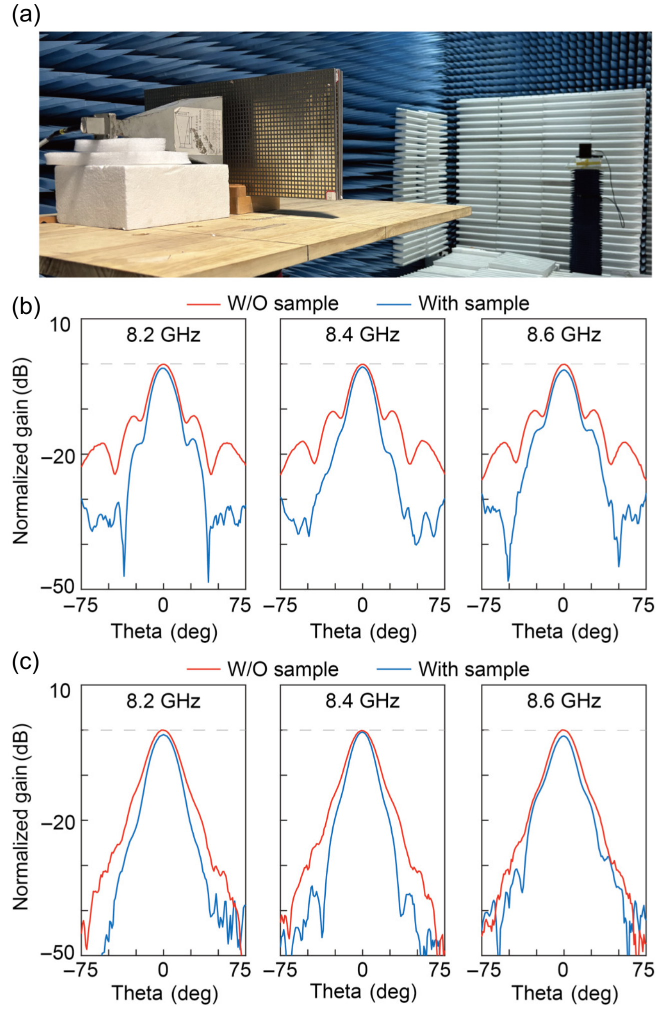

FIG. 10. Measured normalized gain of the horn antenna with and without the cascaded sample: (a) measurement setup, (b) E-plane, and (c) H-plane.

TABLE II. Comparisons with other designs.

Ref.	Modes	Bandwidth	Angular selectivity		Profile (λ_0)
			Passband	Stopband	
[12]	TM	444 THz (<1%)	0°–2°	>6°	>38
[16]	TM	214 THz (<1%)	0°–10°	>15°	>2
[21]	TE, TM	10 GHz (<1%)	0°–10°	0°–10°	0.60
[22]	TE, TM	10.25 GHz (<1%)	0°–15°	26°–85°	0.64
[25]	TE, TM	2.94–3.1 GHz (5%)	0°–15°	>30° 0°–20°	1.15
[26]	TM	400–600 THz (40%)	55°–60°	75°–80°	>18
[29]	TE, TM	10–20 GHz (67%)	0°–10°	>45°	>100
This work	TE, TM	7.1–8.3 GHz (15.56%)	0°–5°	>30°	1

the y-polarized magnetic field. The probe is moved point-by-point using a mechanically controlled scanning system, covering an area of 480×480 mm^2 with a spatial resolution of 6×6 mm^2. As shown in Fig. 9(c), near-normal incidence waves pass through the cascaded structure within the operational bandwidth. At the same time, nearly all incident energy is blocked under oblique incidence, regardless of frequency or polarization. These results confirm that our design can be used as a spatial filter for wireless systems.

Finally, to show the effect of the cascaded sample in suppressing antenna sidelobe, we conducted an experiment that involved placing the composite sample in front of a transmitting antenna and measuring its radiation performance, as shown in Fig. 10(a). The receiving antenna is located 4.6 m from the transmitting antenna, and the turntable rotates in 1° steps. Figures 10(b) and 10(c) show the measured normalized radiation pattern of the transmitting antenna. The red curves represent the patterns without the sample, while the blue curves correspond to the patterns with the sample placed about 4 cm in front of the antenna. To demonstrate broadband performance, we present the measured data at 8.2, 8.4, and 8.6 GHz. At these frequencies, the presence of the sample can suppress the gain levels at large angles. Specifically, at 30°, the suppression at 8.2 GHz is approximately 10 dB in the E-plane and 9 dB in the H-plane. At 8.4 GHz, the suppression is 13 dB in the E-plane and 11 dB in the H-plane. At 8.6 GHz, the E-plane suppression reaches 8 dB, while the H-plane suppression is around 6 dB.

In Table II, we compare our work with related studies, primarily focusing on the polarization behavior, operating bandwidth, angular selectivity, and profile. The comparison illustrates that our method achieves comprehensive performance relative to any other designs.

V. CONCLUSION

We have presented an approach utilizing UZIMs to achieve low-profile, broadband, and polarization-free angular selectivity. The underlying angle-selective mechanism is analyzed through $\boldsymbol{k}$-surface dispersion and phase-matching conditions. The proposed UZIM design integrates a bilayer continuous metallic mesh, SRRs, and I-shaped resonators, enabling 3D dispersion engineering to meet the required constitutive parameter conditions. By cascading multiple UZIM layers with different operating frequencies, the oblique-incidence stopband is significantly broadened to align with the normal-incidence passband, thereby realizing broadband angular selectivity. Experiments are conducted to validate our design. Two application scenarios, i.e., spatial filter and sidelobe suppression, are tested to demonstrate the potential of our design for practical applications. Moreover, the proposed approach can also be extended to higher frequency ranges, such as terahertz frequencies. In such ranges, metals continue to exhibit excellent conductivity. At higher frequencies, the involved metallic electric and magnetic resonators can be replaced with all-dielectric ones [41,42], which is quite promising for realizing high-quality angle-selective optical devices.

ACKNOWLEGEMENT

This work is financially supported by the Natural Science Foundation of China (NSFC) under Grants No. 62471435 and No. 62271439, the Natural Science Foundation of Zhejiang Province (ZJNSF) under Grant No. LZ24F010002, and the Key Research and Development Program of Zhejiang Province under Grant No. 2024C01241(SD2).

Z. H., L. P., Z. W, and D. Y. designed the research; Z. H., L. P., Y. H., X. H., S. Z., X. Z., Z. W., J. T., X. P., and D. Y. performed the research. All the authors contributed to data interpretation and the composition of the manuscript.

DATA AVAILABILITY

The data that support the findings of this article are not publicly available. The data are available from the authors upon reasonable request.

APPENDIX A: DESIGN TRADEOFFS BETWEEN ANGULAR REJECTION RANGE, THE NUMBER OF CASCADED LAYERS, AND THE TOTAL DEVICE THICKNESS

To discuss the tradeoffs among various metrics of our design, we provide a detailed explanation from both the physical modeling and practical design perspectives. Considering the physical mechanism of our design, we interpret that the primary trade-off lies among the angular rejection range, the number of cascaded layers, and the operating bandwidth as follows.

(1) A larger angular rejection range results in a narrower bandwidth. As illustrated in Fig. 11, the frequency spacing is set at $0.025\omega_0$ [Fig. 11(a)] and $0.05\omega_0$ [Fig. 11(b)]. The corresponding rejection angle range (i.e., $|S_{21}| < 0.3$) and bandwidth are 70° and $0.045\omega_0$ and 65° and $0.076\omega_0$, respectively.

(2) The number of metamaterial layers is crucial for achieving a broader bandwidth, as well as a larger rejection angle. As shown in Figs. 11(a) and 11(c), for a fixed angular rejection range, increasing the number of layers effectively extends the bandwidth. Since the stacking of metamaterial layers is quite simple, it is imagined that this operation can be adopted to broaden the bandwidth further and to promote the angular rejection range.

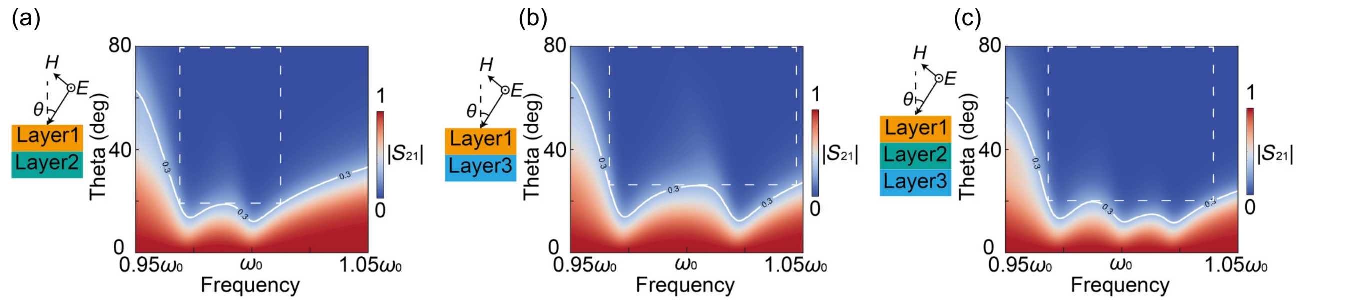

FIG. 11. Simulated angle rejection range (dashed box) under different situations. (a) Layers 1 and 2 combination, with a frequency spacing of $0.025\omega_0$. (b) Layers 1 and 3 combination, with a frequency spacing of $0.05\omega_0$. (c) Three-layer combination, with a frequency spacing of $0.025\omega_0$.

However, the stacking of multiple metamaterial layers is limited due to some practical issues. (i) Considering that the metamaterial layers are composed of metallic structures, the spacing between adjacent layers should be ensured to avoid strong near-field coupling, which also leads to an increase in the total thickness of the whole structure when the number of layers is large. (ii) The operating bandwidth of a single-layer transmissive metasurface under normal incidence imposes a fundamental limit—no matter how many layers are stacked, the overall bandwidth cannot exceed that of a single layer. (iii) The inherent material losses (i.e., ohmic loss in metals and dissipation in dielectrics) will nonlinearly grow with a large number of layers.

APPENDIX B: LOSS IN THE PROPOSED METAMATERIAL

Here, we take the six-layer structure as an example to evaluate the loss condition. In the simulations, the metal adopted is copper with an electrical conductivity of 5×10^7 S/m, and the F4B substrate was modeled with a loss tangent of 0.002. Figure 12 shows the power dissipated by each material under normal incidence. As expected, the power dissipation in both materials remains nearly nondispersive across the whole operating band. On average, copper accounts for 11.2% of the total loss (green curve), while the F4B substrate contributes about 4.5% (red curve).

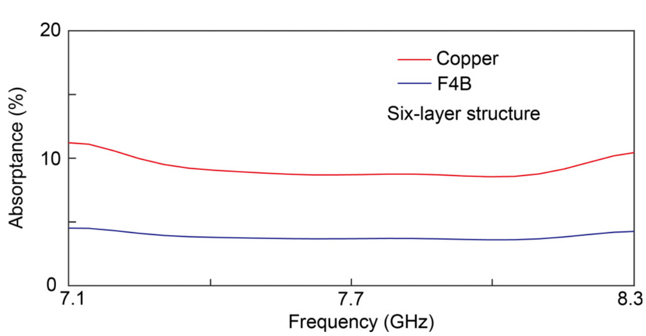

FIG. 12. Simulated power dissipation on copper and dielectric (F4B) for a six-layer structure under normal incidence.

The proposed UZIM requires EM resonance at the deep subwavelength scale, which is currently achieved through complex metallic structures. The lossy metal would dissipate the incident EM power, especially close to the resonant frequencies. A possible method to reduce power loss is to use low-loss dielectrics rather than metals to construct the resonators. The all-dielectric resonators can be quite effective in resembling the EM modes adopted in our metallic structures, which provides the possibility of loss reduction. Hence, it is indeed a good area for future work.

APPENDIX C: GEOMETRIC TOLERANCES OF IN-PLANE DIMENSIONS (*a*, *m*, AND *n*)

Two factors primarily govern the geometric parameter tolerance. The first one is the sensitivity of the structural resonant frequency to the considered geometric parameter. The second one is the spectral proximity between the operating band and the resonant frequency. In our design, the broad passband under normal incidence is spectrally distant from the electric resonance frequency. As a result, the geometric tolerance associated with the electric resonator (continuous metallic mesh) is relatively high. Specifically, the width of the metallic strip in Fig. 3(a) has a comparatively minor influence on the performance. Conversely, the stopband under oblique incidence is introduced via near-zero constitutive parameters and occurs precisely near the resonant frequency. Therefore, the geometric tolerances of the corresponding resonators are relatively tight. In other words, the geometric parameter tolerances of the two structures illustrated in Figs. 3(b) and 3(c) are more critical.

To validate these assertions, we select three key geometric parameters (a, m, and n) and perform simulations to evaluate their impact on performance with a variation of 0.1 mm applied to each. As shown in Fig. 13(a), parameter a primarily influences the passband under normal incidence and is shown to have a limited effect on performance. As displayed in Fig. 13(b), parameter m

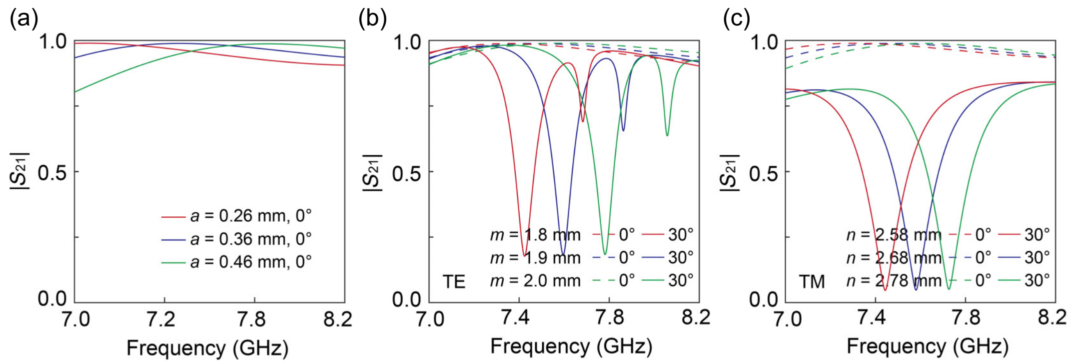

FIG. 13. Simulated $|S_{21}|$ under normal and oblique (30°) incidences with respect to different geometric parameters: (a) a, (b) m, TE waves, and (c) n, TM waves.

mainly affects the normal magnetic resonance and, thus, has a notable influence on the TE-wave stopband under oblique incidence. As shown in Fig. 13(c), parameter n predominantly governs the normal electric resonance and, consequently, affects the TM-wave stopband under oblique incidence.

Although variations in these geometric parameters cause slight shifts in the operating band, the angular selectivity remains largely stable. In PCB processes, fabrication errors are typically significantly below 0.1 mm. Therefore, the performance of the physically fabricated sample aligns closely with the simulated results.

APPENDIX D: OPTIMIZATION OF AIR-GAP THICKNESS AND FREQUENCY SPACING TO ACHIEVE BROADBAND ANGULAR SELECTIVITY

In our design, the air gaps primarily influence two aspects of performance. The first one is the overall profile of the cascaded structure. For a given number of UZIM layers, a thinner air gap results in a smaller overall profile. The second one is the EM mutual coupling between two adjacent layers, which affects the stopband under oblique incidence. The passband for normal incidence is less affected since strong resonance levels occur far beyond this frequency. In contrast, the stopband under oblique incidence occurs close to the resonant frequencies and is sensitive to the gap width. Figure 14 shows the simulated transmission ($|S_{21}|$) of a three-layer structure with varying air-gap thicknesses. The resonant frequencies under oblique incidence (30°) for these three layers are 7.6, 7.8, and 8.0 GHz, respectively. It can be observed that an excessively small air gap degrades the overall stopband performance under oblique incidence, and all three resonant frequencies are shifted. As expected, the air gap has little effect on the passband at normal incidence. In our design, to achieve favorable stopbands at 30° incidence, the air gap was chosen to be 3 mm in thickness, balancing both EM performance and structural profile.

The frequency spacing mainly affects the whole operating bandwidth, as well as the uniformity of angular selectivity across the operating band, for a fixed number of layers. A smaller frequency spacing results in improved uniformity of angular selectivity. Correspondingly, achieving a broader bandwidth requires more layers that, in turn, increase the overall profile. Therefore, the selection of the frequency spacing strikes a balance among the bandwidth, uniformity of angular selectivity, and structural profile. To verify this fact, the angular selectivity performance of the ideal two-layer structures with different frequency spacings (0.2 and 0.6 GHz) is examined, as shown in Fig. 15. As expected, a clear trade-off exists between the uniformity of angular selectivity and operating bandwidth. In our design, aiming for favorable stopband performance and sufficient bandwidth at 30° incidence, the frequency

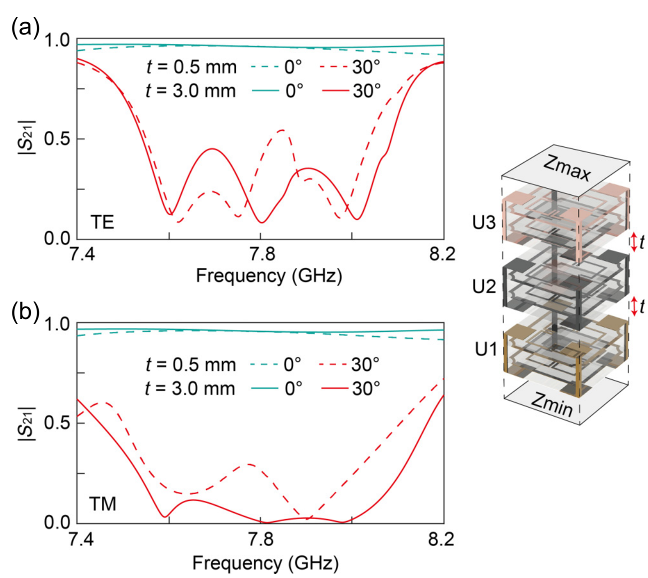

FIG. 14. Simulated $|S_{21}|$ of the three-layer structure at 0° and 30° incidences with different thicknesses of the air gap (0.5 and 3 mm): (a) TE waves and (b) TM waves.

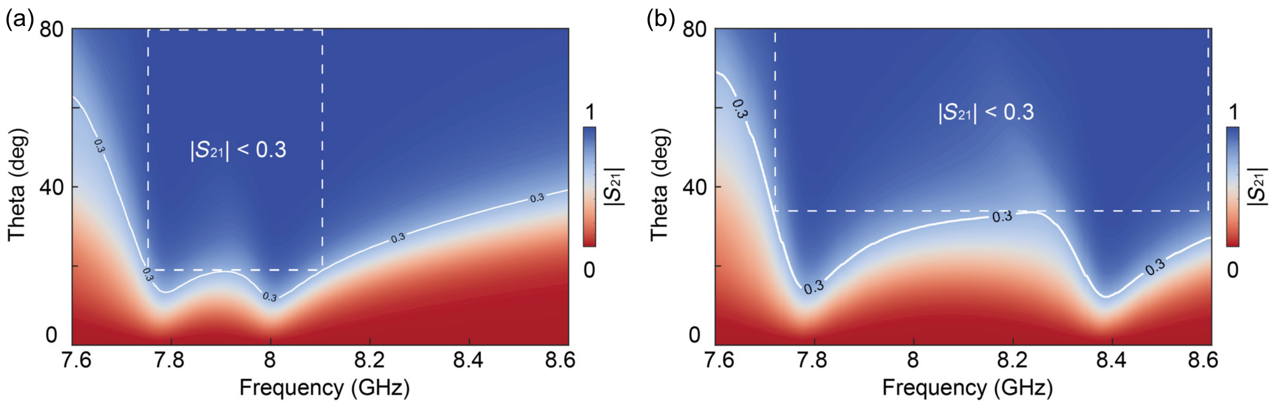

FIG. 15. Simulated $|S_{21}|$ of the two-layer structure with different frequency spacings: (a) 0.2 GHz and (b) 0.6 GHz.

spacing was chosen to be 0.2 GHz. To achieve simultaneous improvement in both the uniformity of angular selectivity and bandwidth, we can reduce the frequency spacing while increasing the number of layers.

[1] Q. Lou and Z. Chen, Sidelobe suppression of metalens antenna by amplitude and phase controllable metasurfaces, IEEE Trans. Antennas Propag. **69**, 6977 (2021).

[2] L. Wu, N. Zhang, K. Qu, K. Chen, T. Jiang, J. Zhao, and Y. Feng, Transmissive metasurface with independent amplitude/phase control and its application to low-side-lobe metalens antenna, IEEE Trans. Antennas Propag. **70**, 6526 (2022).

[3] T. Han, B. Dong, Y. Zhang, Y. Wang, Z. Yan, H. Zhou, J. Feng, and Y. Liu, Research on the radiation properties of tapered slot magnetoelectric antenna, Prog. Electromagn. Res. **177**, 75 (2023).

[4] S. Lian, W. Hu, X. Song, and Z. Liu, Smart privacy-preserving screen based on multiple sensor fusion, IEEE Trans. Consum. Electron. **59**, 136 (2013).

[5] D. Li, X. Hu, B. Gao, W. Yin, H. Chen, and H. Qian, Highly transparent tunable microwave perfect absorption for broadband microwave shielding, Prog. Electromagn. Res. **176**, 35 (2023).

[6] P. Bermel, Michael Ghebrebrhan, Walker Chan, Yi Xiang Yeng, Mohammad Araghchini, Rafif Hamam, Christopher H. Marton, Klavs F. Jensen, Marin Soljačić, John D. Joannopoulos, *et al.*, Design and global optimization of high-efficiency thermophotovoltaic systems, Opt. Express **18**, A314 (2010).

[7] L. Guo, J. Li, W. Huang, H. Shao, T. Ba, T. Jiang, Y. Jiang, and G. Deng, Waveguide magic-t with coplanar arms for high-power solid-state power combining, IEEE Trans. Microwave Theory Tech. **65**, 2942 (2017).

[8] L. Guo, J. Li, W. Huang, H. Shao, S. Xie, G. Deng, Y. Zhang, and J. Ren, A high-isolation eight-way power combiner, IEEE Trans. Microwave Theory Tech. **68**, 854 (2020).

[9] L. Guo, G. Deng, S. Xie, H. Shao, W. Huang, Y. Zhang, Y. Zhang, and M. Tong, A miniaturized high-power integrated front-end for phased array antenna, IEEE Trans. Compon., Packag., Manuf. Technol. **13**, 1770 (2023).

[10] J. H. Atwater, P. Spinelli, E. Kosten, J. Parsons, C. Van Lare, J. Van de Groep, J. G. de Abajo, A. Polman, and H. A. Atwater, Microphotonic parabolic light directors fabricated by two-photon lithography, Appl. Phys. Lett. **99**, 151113 (2011).

[11] E. D. Kosten, J. H. Atwater, J. Parsons, A. Polman, and H. A. Atwater, Highly efficient gaas solar cells by limiting light emission angle, Light: Sci. Appl. **2**, e45 (2013).

[12] P. Huo, Y. Liang, S. Zhang, Y. Lu, and T. Xu, Angular optical transparency induced by photonic topological transitions in metamaterials, Laser Photonics Rev. **12**, 1700309 (2018).

[13] X. Jiang, T. Wang, L. Cheng, Q. Zhong, R. Yan, and X. Huang, Tunable optical angular selectivity in hyperbolic metamaterial via photonic topological transitions, Opt. Express **27**, 18970 (2019).

[14] Z. Su and Y. Wang, Anisotropic photonics topological transition in hyperbolic metamaterials based on black phosphorus, Nanomaterials **10**, 1694 (2020).

[15] Y. He, K. Xu, Y. Wu, R. Zhang, G. Liu, and J. Li, Optical angular transparency and broadband absorption based on photonic topological transition in black phosphorus/aluminum oxide hyperbolic metamaterial, AIP Adv. **13**, 015301 (2023).

[16] P. Moitra, Y. Yang, Z. Anderson, I. I. Kravchenko, D. P. Briggs, and J. Valentine, Realization of an all-dielectric zero-index optical metamaterial, Nat. Photonics **7**, 791 (2013).

[17] J. D. Ortiz, J. D. Baena, V. Losada, F. Medina, and J. L. Araque, Spatial angular filtering by fsss made of chains of interconnected SRRS and CSRRS, IEEE Microwave Wireless Compon. Lett. **23**, 477 (2013).

[18] L. Zhou and Z. Shen, Angular selectivity based on a double-resonance periodic array of scatterers, Opt. Express **29**, 20379 (2021).

[19] N. Kou and S. Yu, Angular selectivity based on odd mode resonance of frequency selective surface, IEEE Antennas Wireless Propag. Lett. **21**, 2151 (2022).

[20] Z. Wang, X. Yang, Z. Zong, W. Wu, and D. Fang, Design of low-profile single-layer angle-selective surfaces based

on the first odd mode resonance, IEEE Trans. Antennas Propag. **72**, 4624 (2024).

[21] C. Du, H. Chen, S. Wang, Y. Pang, T. Zhou, S. Xia, and D. Zhou, Dual-polarized angle-selective surface based on double-layer frequency selective surface, Appl. Phys. Lett. **124**, 111701 (2024).

[22] Y. Hong and Z. Shen, Dual-polarized bilayer angle-selective structure, IEEE Antennas Wireless Propag. Lett. **23**, 823 (2024).

[23] C. Niu, J. Zhao, L. Du, N. Liu, Z. Wang, W. Huang, and X. Li, Spatially dispersive dichroism in bianisotropic metamirrors, Appl. Phys. Lett. **113**, 261102 (2018).

[24] X. Chen, Z. Wang, W. Chen, Y. Ang, W. Yin, H. Chen, and E. Li, Magnetic metamirrors as spatial frequency filters, IEEE Trans. Antennas Propag. **68**, 5505 (2020).

[25] Z. Chen, C. Du, J. Liu, D. Zhou, and Z. Shen, Design methodology of dual-polarized angle-selective surface based on three-layer frequency-selective surfaces, IEEE Trans. Antennas Propag. **71**, 8704 (2023).

[26] Y. Shen, D. Ye, I. Celanovic, S. G. Johnson, J. D. Joannopoulos, and M. Soljacic, Optical broadband angular selectivity, Science **343**, 1499 (2014).

[27] Y. Shen, D. Ye, L. Wang, I. Celanovic, L. Ran, J. D. Joannopoulos, and M. Soljacic, Metamaterial broadband angular selectivity, Phys. Rev. B **90**, 125422 (2014).

[28] Y. Qu, Y. Shen, K. Yin, Y. Yang, Q. Li, M. Qu, and M. Soljacic, Polarization-independent optical broadband angular selectivity, ACS Photonics **5**, 4125 (2018).

[29] Y. Gao, B. Li, R. Wang, Q. Yan, J. Huangfu, and D. Ye, Polarization-independent broadband angular selectivity based on anisotropic diamagnetic metamaterial, IEEE Trans. Antennas Propag. **70**, 7306 (2022).

[30] J. B. Pendry, A. J. Holden, W. J. Stewart, and I. Youngs, Extremely low frequency plasmons in metallic mesostructures, Phys. Rev. Lett. **76**, 4773 (1996).

[31] J. B. Pendry, A. J. Holden, D. J. Robbins, and W. J. Stewart, Magnetism from conductors and enhanced nonlinear phenomena, IEEE Trans. Microwave Theory Tech. **47**, 2075 (1999).

[32] Y. He and G. V. Eleftheriades, A thin double-mesh metamaterial radome for wide-angle and broadband applications at millimeter-wave frequencies, IEEE Trans. Antennas Propag. **68**, 2176 (2020).

[33] Z. Chu, T. Li, J. Wang, Y. Han, R. Zhu, T. Cui, and S. Qu, Ultrawide-angle broadband electromagnetic window for both TM-and TE-polarizations by synergy of multi-mechanism resonances, IEEE Trans. Microwave Theory Tech. **71**, 3701 (2023).

[34] F. Ding, Y. Cui, X. Ge, Y. Jin, and S. He, Ultra-broadband microwave metamaterial absorber, Appl. Phys. Lett. **100**, 103506 (2012).

[35] Y. Li, P. Gu, Z. He, Z. Cao, J. Cao, K. W. Leung, and D. Ding, An ultra-wideband multilayer absorber using an equivalent circuit-based approach, IEEE Trans. Antennas Propag. **70**, 11911 (2022).

[36] D. Wang, X. Cui, D. Liu, X. Zou, G. Wang, B. Zheng, and T. Cai, Multi-characteristic integrated ultra-wideband frequency selective rasorber, Prog. Electromagn. Res. **179**, 49 (2024).

[37] X. Chen, T. M. Grzegorczyk, B. I. Wu, J. Pacheco, and J. A. Kong, Robust method to retrieve the constitutive effective parameters of metamaterials, Phys. Rev. E **70**, 016608 (2004).

[38] T. Li, Y. Fan, Y. Gu, S. Zhou, P. Qin, D. Li, W. Sha, and E. Li, A novel miniaturized multiband strong coupled-FSS structure insensitive to almost all angles and all polarizations, IEEE Trans. Antennas Propag. **69**, 8470 (2021).

[39] J. Luo, Y. Yang, Z. Yao, W. Lu, B. Hou, Z. H. Hang, C. T. Chan, and Y. Lai, Ultratransparent media and transformation optics with shifted spatial dispersions, Phys. Rev. Lett. **117**, 223901 (2016).

[40] Q. Lv, C. Jin, B. Zhang, L. Yin, S. Liu, B. Tian, and T. Cui, Ultrawide-angle ultralow-reflection phenomenon for transverse electric mode in anisotropic metasurface, Adv. Opt. Mater. **10**, 2102400 (2022).

[41] T. Dong, J. Liang, S. Camayd-Muñoz, Y. Liu, H. Tang, S. Kita, P. Chen, X. Wu, W. Chu, E. Mazur, and Y. Li, Ultra-low-loss on-chip zero-index materials, Light: Sci. Appl. **10**, 10 (2021).

[42] H. Tang, C. DeVault, S. A. Camayd-Muñoz, Y. Liu, D. Jia, F. Du, O. Mello, D. Vulis, Y. Li, and E. Mazur, Low-loss zero-index materials, Nano Lett. **21**, 914 (2021).